

Article

Numerical Modelling and Experimental Validation of Novel Para Winglet Tape for Heat Transfer Enhancement

Thejaraju Rajashekaraiyah ^{1,2}, Girisha Kanuvanahalli Bettaiah ³ , Parvathy Rajendran ^{4,5,*} ,
Mohamed Abbas ^{6,7,8} , Sher Afghan Khan ⁹ and C. Ahamed Saleel ¹⁰ 

- ¹ Department of Mechanical Engineering, Visvesvaraya Technological University, Belgaum 590018, Karnataka, India
- ² Department of Mechanical Engineering, School of Engineering and Technology, CHRIST (Deemed to Be University), Bengaluru 560076, Karnataka, India
- ³ Department of Mechanical Engineering, BGSIT-Adichunchanagiri University BG Nagara, Javarana Hally 571448, Karnataka, India
- ⁴ School of Aerospace Engineering, Universiti Sains Malaysia, Engineering Campus, Nibong Tebal 14300, Pulau Pinang, Malaysia
- ⁵ Faculty of Engineering Computing, First City University College, Bandar Utama, Petaling Jaya 47800, Selangor, Malaysia
- ⁶ Electrical Engineering Department, College of Engineering, King Khalid University, Abha 61421, Saudi Arabia
- ⁷ Electronics and Communications Department, College of Engineering, Delta University for Science and Technology, Gamasa 35712, Egypt
- ⁸ Research Center for Advanced Materials Science (RCAMS), King Khalid University, P.O. Box 9004, Abha 61413, Saudi Arabia
- ⁹ Department of Mechanical Engineering, Faculty of Engineering, International Islamic University, Kuala 44000, Lumpur, Malaysia
- ¹⁰ Department of Mechanical Engineering, College of Engineering, King Khalid University, P.O. Box 394, Abha 61421, Saudi Arabia
- * Correspondence: aeparvathy@usm.my



Citation: Rajashekaraiyah, T.; Bettaiah, G.K.; Rajendran, P.; Abbas, M.; Khan, S.A.; Saleel, C.A. Numerical Modelling and Experimental Validation of Novel Para Winglet Tape for Heat Transfer Enhancement. *Mathematics* **2022**, *10*, 2893. <https://doi.org/10.3390/math10162893>

Academic Editors: Yuan Dong and Yuchao Hua

Received: 18 July 2022

Accepted: 8 August 2022

Published: 12 August 2022

Publisher's Note: MDPI stays neutral with regard to jurisdictional claims in published maps and institutional affiliations.



Copyright: © 2022 by the authors. Licensee MDPI, Basel, Switzerland. This article is an open access article distributed under the terms and conditions of the Creative Commons Attribution (CC BY) license (<https://creativecommons.org/licenses/by/4.0/>).

Abstract: Heat exchangers are predominantly used in the industries of production, manufacturing, power, oil and gas, petroleum, and cooling solutions. The competence of the heat exchanger is optimized through active and passive augmented techniques. The current study revolves around the performance evaluation of Novel Para winglet tape for flow and friction characteristics. Turbulence flow properties from Re of 30,000-to-6000 were explored for three different inclinations and pitches, respectively. Experimental and numerical solutions are derived to showcase the flow behavior over Para winglet tape inserts in the double pipe heat exchanger. Appreciable results were obtained in enhancing the Nusselt number (Nu_p) for a better heat transfer enforcement through the DEX. All case studies also increased when compared to the smooth pipe. Experimentally, the maximum Nu and Nusselt number ratio was observed to be 398.23 and 5.05 times over the plain tube. Similarly, the maximum friction factor and its ratio were observed to be near 0.33 and 8.89 times over the plain tube. Finally, the maximum POI of 2.68 to 2.37 was achieved with 20° inclinations. The experimental and numerical outcomes of Para winglet tape with the higher inclination and shorter pitch were found to be best out of the others.

Keywords: heat exchangers; performance evaluation; experimental; numerical

MSC: 65K05; 65L09

1. Introduction

The heat exchanger is one of a few important types of equipment that have found themselves in the application [1] of pharmaceutical, refrigeration, medical waste recycling, heat recovery systems [2], energy systems, automobile, and aeronautical industries [3]. Engineers in industries are very keen on energy savings and the performance of equipment.

Optimization techniques (OT) can serve as one of the break-throughs for their needs in long-term conditions. The heat transfer rate and pressure drop [4] or, in other words, the Nusselt number (Nu_p) [5] and the friction coefficient, are used to assess the efficacy of OT [6]. Passive and active strategies are used to characterize OT. Recent findings on the OT [7] from numerous researchers on double pipe heat exchangers (DHX) [8,9] are shown in Table 1 to describe their achievements.

Table 1. Optimization Techniques in DHX.

Sl. No.	Author	Type of OT	Achievements
1	Zheng [10]	HEV vortices generator	Generates longitudinal vortices
2	Mozafarie [11]	Circular fin	Efficiency optimized to 15%
3	Liu [12]	Fluid exchange inserts	Efficiency optimized to 24% \approx 64%
4	Maakoul [13]	helical baffle	Deficiency of 10 to 15%
5	Shiva Kumar [14]	parabolic fin and triangular fins	Pressure drop and fin effectiveness increased compared to plain tube
6	Huang [15]	Y-branch inserts	17% to 122% was optimized in heat transfer
7	Wijayanta [16]	delta-wing tape inserts	A maximum of 15% enhancement was achieved
8	Salem [17]	helical tape insert	Efficiency optimized to 30% to 95%
9	Mashoofi [18]	axially perforated twisted tapes	A maximum of 7% enhancement was achieved
10	Pourahmad [19]	wavy strip	Effectiveness has increased from 15 to 70%
11	Sheikholeslami [20]	Discontinuous helical turbulators	Efficiency optimized to 5% to 50%
12	Sheikholeslami [21]	perforated circular-ring	Efficiency optimized to 10% to 20%
13	Zohir [22]	Coiled wires	Effectiveness has increased from 20 to 100%
14	Naphon [23]	Brush Inserts	Pressure drop and effectiveness increased compared to plain tube
15	Zhang [24]	Vortex generators	Heat transfer was enhanced to 1.34 to 1.46 times

Table 1 shows a different set of inserts and their optimization levels with the flow for the past decade. The study of Y-branch inserts by Huang [15], and Vortex generators by Zhang [24] has achieved the highest augmentation of heat transfer in the flow regime. The investigation of the wavy strip and coiled wires by Pourahmad [19] and Zohir [22] has proved to have an effectiveness of 70% to 100%. The fluid flow assessment in a square and circular heat exchanger was investigated by Abdelrazek [25]. They used four different types of nanofluids mixed in distilled water. Both experimental and numerical analyses were carried out by them. They found the different percentages of enhancement in heat transfer rates when the same fluid is passed into the circular and square heat exchangers. Afzal [26] used graphene nanofluid in water (base fluid) to investigate the heat transfer performance of a novel implanted helical tube type triple heat exchanger. The nanofluid concentration, flow rate of hot water, and cold water were all varied during the experiments. They found considerable variations in the Nusselt numbers in this heat exchanger as compared to a normal concentric pipe exchanger. A significant enhancement in heat transfer coefficients was also found by using the nanofluids as compared to pure water.

Noorbakhsh [27] investigated the influence of employing distorted tapes of different shapes on both the tubes of a concentric tube heat exchanger. The investigation was conducted using commercially available CFD software ANSYS Fluent V18. The effect of various parameters on the thermal performance of the exchanger was analyzed by determining the exit temperature, Nusselt number, and pressure drop. They found an increment in the Nusselt number due to the increment in the number of twisted tapes from 1 to 4. There was also a reduction in pressure drop for this configuration. Hosseinnejad et al. [28] numerically investigated the heat transfer features of tubular-type heat exchangers

that had dual distorted tapes. The flow was maintained as turbulent, with constant inlet velocity. They used commercially available CFD code Fluent to solve the governing equations. The results showed that aligned positioning improves heat transfer performance more than non-aligned positioning. The investigation concerning the air–air heat exchanger on any OT is very limited. So, the current investigation was carried out between Reynolds number 30,000 and 6000 with the application of Para-Winglet Tape (PWT) for the tube section. The PWT was investigated with CFD results and correlations were developed for flow and thermal parameters. The present study involved the development of a new type of turbulator/swirl generator for optimizing the performance of heat exchangers in terms of Nusselt number, friction factor, performance optimization index, and effectiveness. An air-to-air double pipe heat exchanger test setup was developed to investigate the PWT Inserts with 10° , 15° , and 20° degrees of para-inclination for dimensionless Reynolds numbers fluctuating between 6000 and 30,000.

2. Investigation Details

Figure 1 provides the details of the investigating setup developed for the experimentation of PWT. The flow was developed using the blowers and u-tube manometers were used to validate the pressure, settling tank for the stabilization of flow, surface heat for the addition of heat, DAC system to monitor the temperature readings, and inverter to reduce the fluctuations of power. The shell section was completely insulated with glass wool and asbestos rope. The tube section was made of copper for better heat engagements.

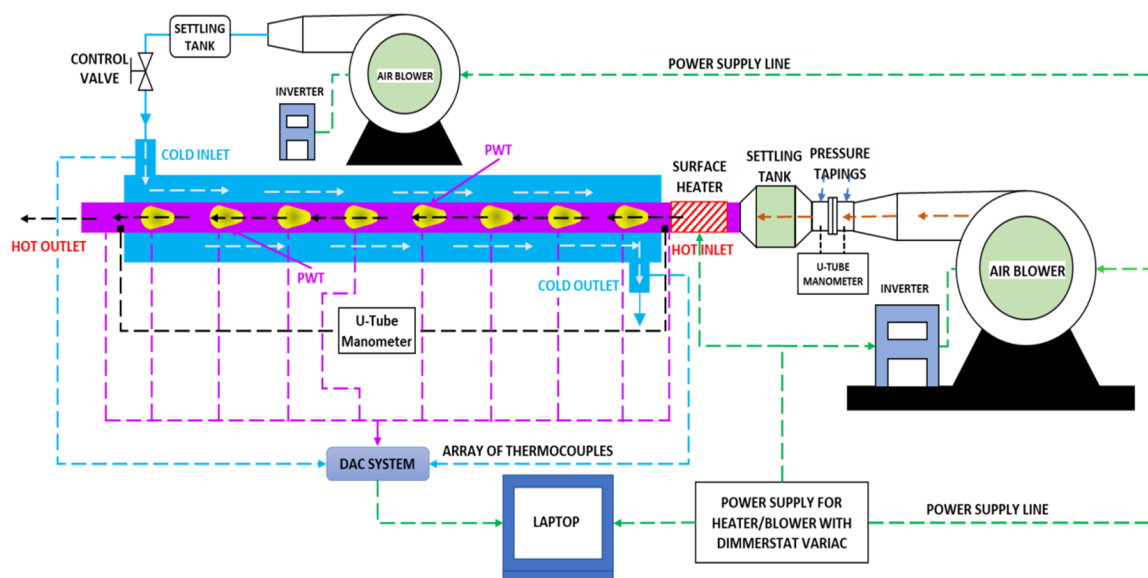


Figure 1. DHX Investigation Setup [29].

The design of the PWT inserts is shown in Figure 2. The designs were developed to achieve better heat transfer over the smooth tube at a turbulent flow regime. They were placed in tube sections securely and monitored the surface temperature through ten evenly placed K-type thermocouples. The design of PWT is similar to that of a parachute design. The survey shows that inserts are manufactured with a material that is tough, flexible, and easy to manufacture. Stainless steel is one such type of material that has the above properties.

The development of the PWT was carried out with utmost care so as minimize any errors from the external environment. Figure 2 shows that the PWT inserts displayed at different pitches and inclinations. Figure 3a displays the orientation of the PWT by showcasing the pitch of three variants, namely 30 mm, 40 mm, and 50 mm. Figure 3b displays the orientation of the PWT by showcasing the para inclinations of three variants, namely 10° , 15° , and 20° degrees. The thermophysical characteristics of the tube material

(copper), the hot stream in the tube, and the cold fluid across the annular portion are described in Table 2.

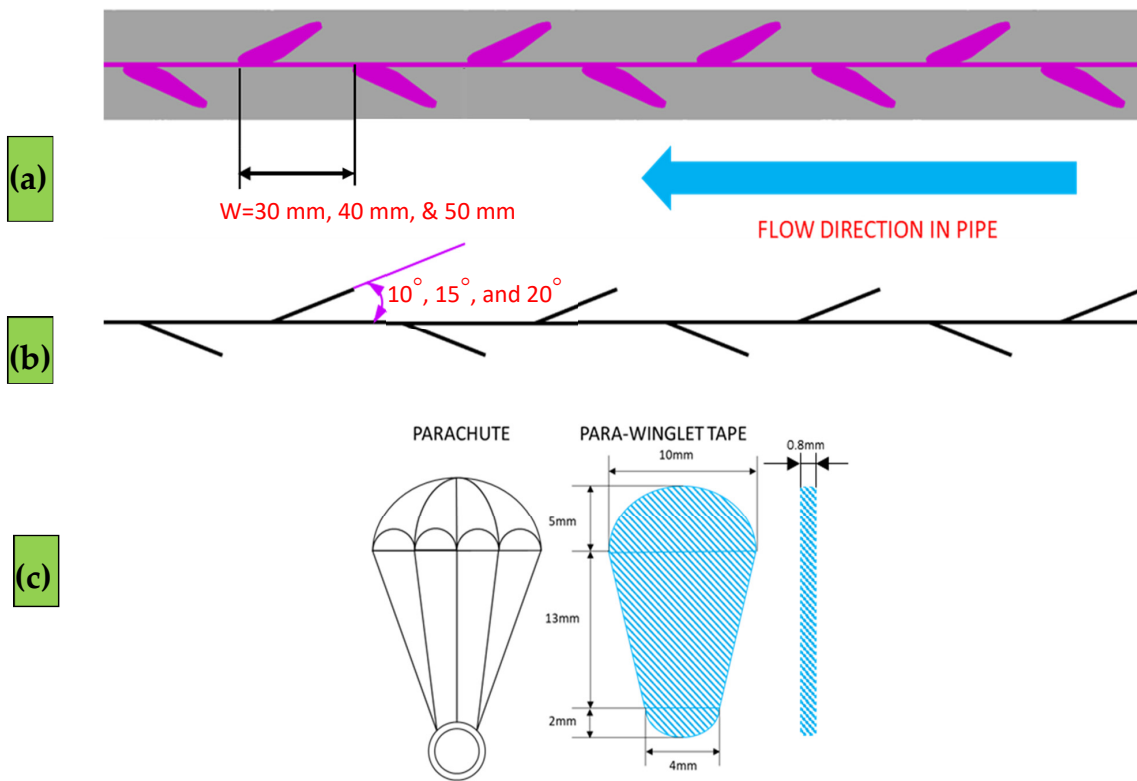


Figure 2. (a) Positioning of PWT inserts inside tube (b) Angle Orientation of PWT inserts (c) Design of Single PWT [29].

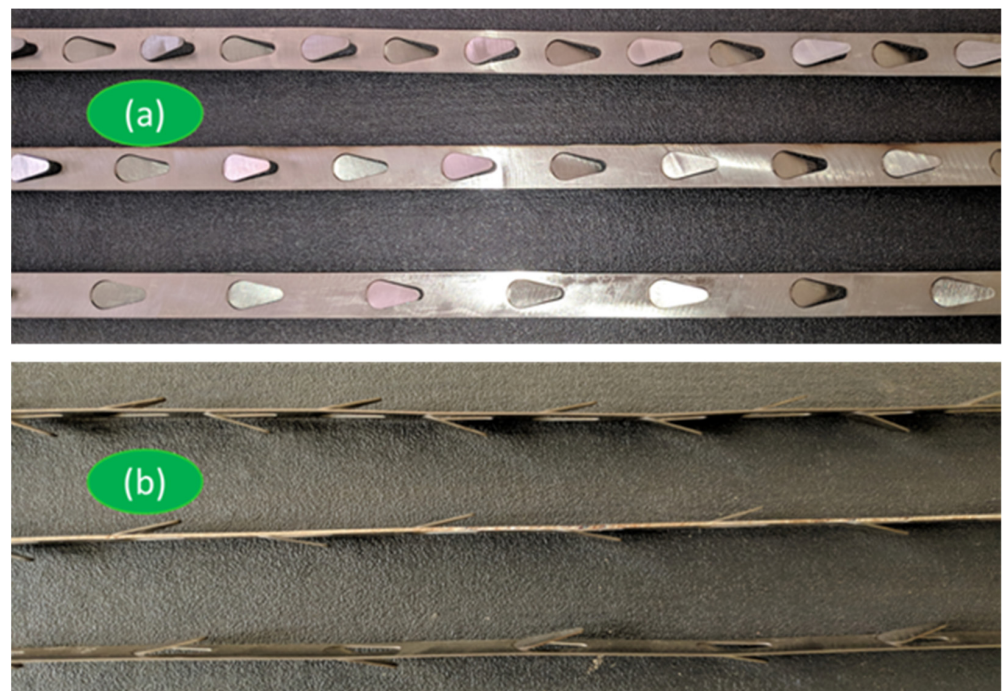


Figure 3. (a) Top View of the PWT with different pitches (b) Side view of the PWT with different inclinations [29].

Table 2. Thermophysical properties.

Type	Temperature in [K]	C_p in [J/KgK]	ρ in [Kg/m ³]	μ in [Pa·S]	K in [W/mk]	Pr
Hot Fluid	300	1007.07	1.16134	18.568×10^{-6}	26.19×10^{-3}	0.7138
Cold Fluid	353	1010.38	0.9869	21.037×10^{-6}	29.99×10^{-3}	0.7083
Copper	—	393.5	8910	—	391.1	—

From Figure 4A it is observed that the numerical model was developed with a boundary layer mesh technique. A 15-layer boundary was developed over the tube surface with a y -plus equal to one to capture the near boundary phenomenon and the exact flow regime is shown in Figure 4B. Figure 4C shows the placement of inserts in the double pipe heat exchanger.

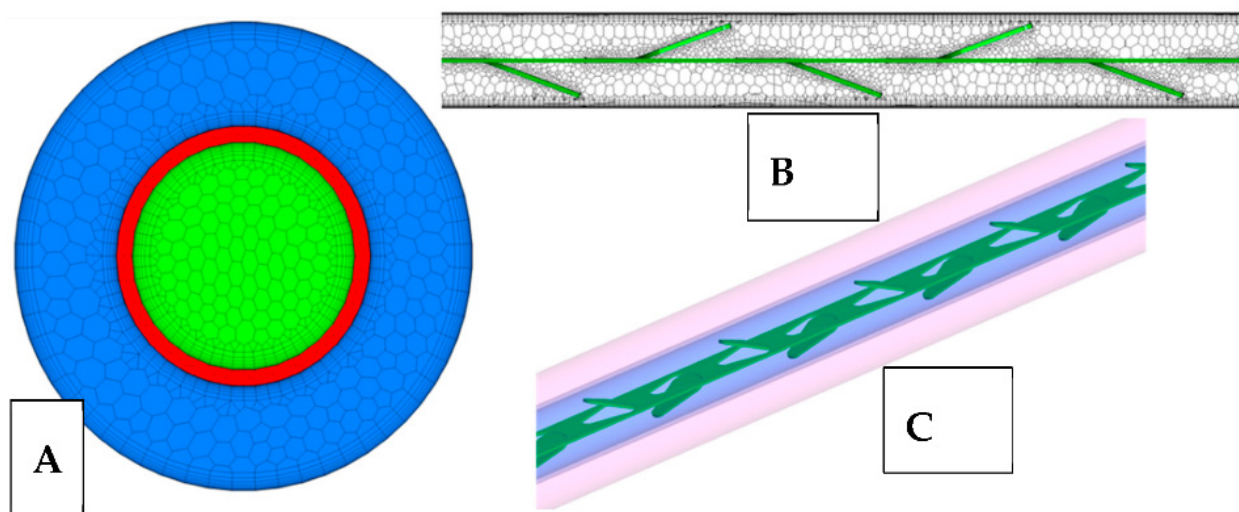


Figure 4. (A) Cross-Sectional view of Numerical Model (B) Longitudinal view of Numerical Model (C) 3D-View of placement of PWT in heat exchanger tube.

The pre-processing, solving, and post-processing steps were carried out using the StarCCM+ software which includes geometry development, mesh development in polyhedral, boundary conditions, inlet conditions, environmental conditions, and post-processing. Polyhedral mesh is considered due to its advantage over the tetrahedral as it takes less CPU time to solve, is more robust for turbulence models, and has fewer internal memory requirements for each case study. Grid independence analysis is usually carried out to understand the number of elements required to reach approximated results of a particular physics. Figure 5 shows the independence check from 11 lakhs to 61 lakhs grid sizes where the heat transfer coefficient and the Nusselt number of the inside tube were measured at each level. The variation in the variable values was seen to be below 2% from 40 lakhs to 61 lakhs. So, a 61 lakhs grid size was selected to study all the cases for numerical simulation.

Figure 6 shows the details of the percentage of heat loss across the insulation from the external surfaces; the variations are high as the Re increases so the maximum possible heat loss, which can be restricted by the insulation provided over the external surfaces, is within 4.7%.

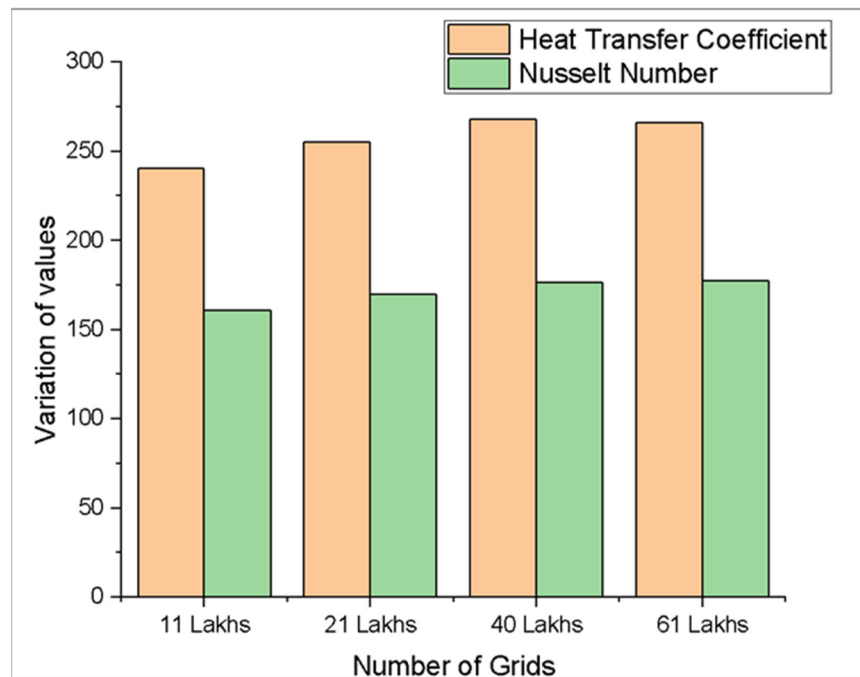


Figure 5. Grid independence analysis.

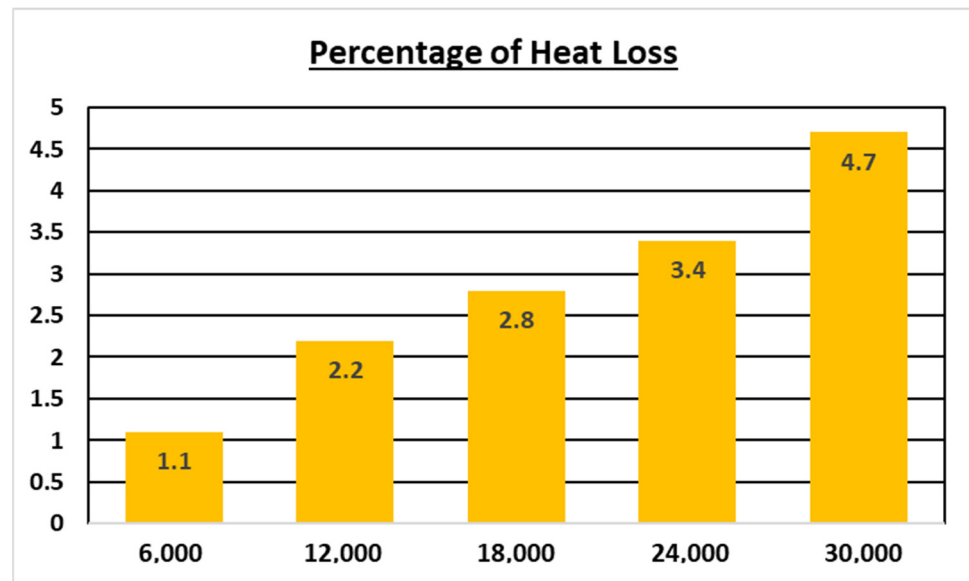


Figure 6. Percentage of Heat Loss across different Re.

3. Data Reduction

From Table 3, “i” and “o” indicate the inlet and exit, “c” and “h” indicate the cold and hot, and “p” and “w” indicate plain and augmented tube. The equations in Table 3 represent the data reduction from temperature, heat transfer, and heat loss to coefficients, dimensionless number, and performance index. Each equation serves as input for the other equation until it has attained the ultimate factor. The data reduction is followed for both augmented pipe and non-augmented pipe concerning different Reynolds numbers as mentioned earlier [30–34]. The relation starts from the temperature, mass flow rate of both hot and cold side fluids, and thermophysical properties of the fluids and solids used in the system as the input variables. Through the relations’ average and overall heat transfer coefficients, heat transfer on the hot and cold side, dimensionless number, and finally the optimization factor is derived for the overall analysis of the DHX [35–38].

Table 3. Numerical and Experimental Correlations.

Sl. No.	Parameters	Notation	Equations
1	Temperature of the hot tube section	T_h	$T_h = \frac{T_{hi} + T_{ho}}{2}$
2	Temperature of cold tube section	T_c	$T_c = \frac{T_{ci} + T_{co}}{2}$
3	heat transfer in cold fluid	Q_c	$Q_c = \dot{m}_c C_{pc} (T_{c,o} - T_{c,i}) = h_o A_o (\bar{T}_{w,avg} - T_c)$
4	Average wall temperature	$\bar{T}_{w,avg}$	$\bar{T}_{w,avg} = \frac{\sum T_{w,o}}{10}$
5	heat transfer in hot fluid	Q_h	$Q_h = \dot{m}_h C_{ph} (T_{h,i} - T_{h,o}) = U_i A_i \Delta_{LMTD}$
6	Logarithmic mean temperature difference	Δ_{LMTD}	$\Delta_{LMTD} = \frac{(T_{h,i} - T_{c,o}) - (T_{h,o} - T_{c,i})}{\ln((T_{h,i} - T_{c,o}) / (T_{h,o} - T_{c,i}))}$
7	Heat loss	Q_{loss}	$Q_{loss} = Q_h - Q_c$
8	Average heat transfer	Q_{avg}	$Q_{avg} = U_i A_i \Delta_{LMTD}$
9	overall heat transfer coefficient	U_i	$\frac{1}{U_i A_i} = \frac{1}{h_i A_i} + \frac{\ln(d_o/d_i)}{2\pi k_p L_i} + \frac{1}{h_o A_o}$
10	heat transfer coefficient tube	h_i	$h_i = \frac{1}{\left[\frac{1}{U_i} - \frac{d_i \ln(d_o/d_i)}{2k_p} - \frac{d_i}{d_o h_o} \right]}$
11	Nusselt Number tube	Nu_p	$Nu_p = \frac{h_i d_i}{k}$
12	Friction factor tube	f_p	$f_p = \frac{\Delta P}{(\rho U^2/2)(L_i/d_i)}$
13	Performance optimization index	POI	$POI = \frac{Nu_w/Nu_p}{(f_w/f_p)^{1/3}}$

4. Governing Equations

The current fluid region is simulated using the CFD approach. The approach is based on three governing equations: continuity, momentum, and energy. The continuity equation denotes mass conservation, the momentum equation denotes force conservation, and the energy equation denotes energy conservation (temperature). For capturing the turbulence performance in the DHX, i.e., $k \rightarrow$ kinetic energy and $\varepsilon \rightarrow$ dissipation correlations are computed concerning the Navier–Stokes equation for stable results on the steady flow heat transfer model. The physics of the numerical model are simulated using the governing equations as shown in Table 4.

Table 4. Governing CFD Correlations.

Sl. No.	Parameters	Notation	Equations
1	Continuity Equation	-	$\frac{\partial}{\partial x_i} (\rho u_i) = 0$
2	Momentum Equation	-	$\frac{\partial}{\partial x_i} (\rho u_i u_k) = \frac{\partial}{\partial x_i} \left(\mu_f \frac{\partial u_k}{\partial x_i} \right) - \frac{\partial p}{\partial x_k}$
3	Energy Equation	-	$\frac{\partial}{\partial x_i} (\rho u_i T) = \frac{\partial}{\partial x_i} \left(\frac{\Gamma}{C_p} \frac{\partial T}{\partial x_i} \right)$
4	Kinetic Energy	k	$\frac{\partial}{\partial x_i} (\rho u_i k) = \frac{\partial}{\partial x_j} \left\{ \left[\frac{\mu_t}{\sigma_k} + \mu \right] \frac{\partial k}{\partial x_i} \right\} + G_k - \rho \varepsilon$
5	Dissipation	ε	$\frac{\partial}{\partial x_i} (\rho u_i \varepsilon) = \frac{\partial}{\partial x_i} \left\{ \left[\frac{\mu_t}{\sigma_\varepsilon} + \mu \right] \frac{\partial \varepsilon}{\partial x_i} \right\} + \frac{\varepsilon}{k} [C_{1\varepsilon} G_k - \rho C_{2\varepsilon} \varepsilon]$

Grid sensitivity checks are usually performed for three main reasons: (a) repeatability of results; (b) computational cost; and (c) computational time. The grid sensitivity check was carried out under the steady-state-turbulence-heat transfer condition where each equation of flow, energy, momentum, and turbulence are validated up to the residual level of 1×10^{-6} . All the equations were solved under the segregated flow conditions

of starccm+ CFD software [39,40]. The grid sensitivity analysis was carried out for 20° inclination and 50 mm pitch over Reynolds numbers of 18,000 for grid sizes 1,134,031, 2,155,673, 4,045,608, and 6,107,308 are presented in Table 5. The interior tube was analyzed for any variations and repeatability in Nusselt number and heat transfer coefficient. The variation between 4,045,608 and 6,107,308 results was less than 2%. So, 4,045,608 grid-level methodologies were implemented for all the other numerical models with changes in the flow conditions.

Table 5. Grid Sensitivity over Reynolds number of 18,000 for 20° inclination and 50 mm pitch.

Number of Cells	1,134,031	2,155,673	4,045,608	6,107,308
h_i	240.34	255.19	267.79	266.15
Nu_p	160.55	169.62	176.24	177.13

5. Discussion of Results

The plain tube was tested with two correlations, mainly Dittus for Nusselt number (Nu_p) and Blasius for friction factor. The correlations are as follows;

$$Dittus - Boelter\ correlation - Nu = 0.023 Re^{0.8} Pr^{0.4} \tag{1}$$

$$Blasius's\ correlation - f = 0.316 Re^{-0.25}. \tag{2}$$

The variation of the test data and numerical data of Nusselt number for a plain tube model was examined and is displayed in Figure 7. The study reveals that the Nusselt number between experimental and numerical values had a maximum variation percentage of ±4.21%. In a similar practice, the friction factor was also determined for experimental and numerical study and observed a maximum variation percentage of ±2.16% in Figure 8. The plain tube analysis provides a clear vision of the approaches between numerical and experimental studies.

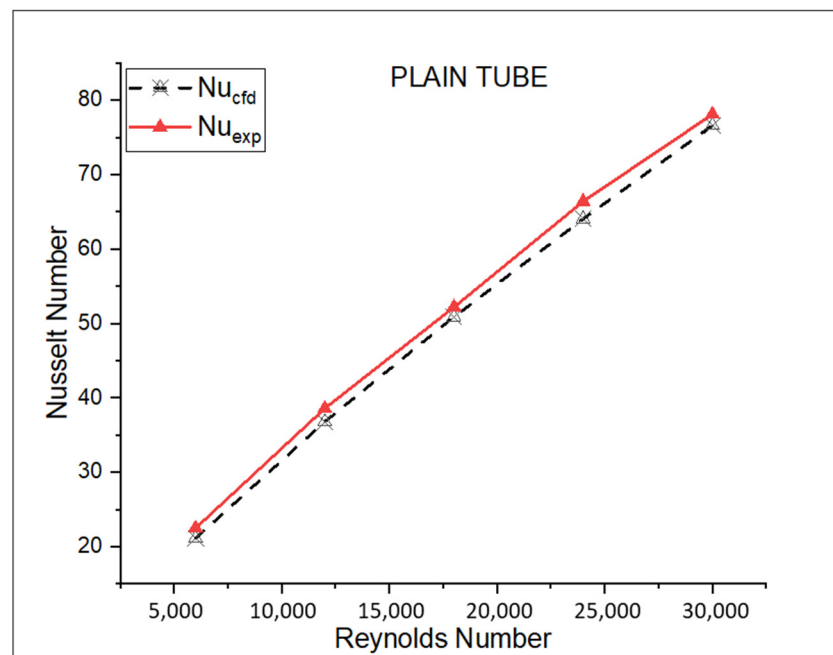


Figure 7. Study of Nu over Reynolds Number.

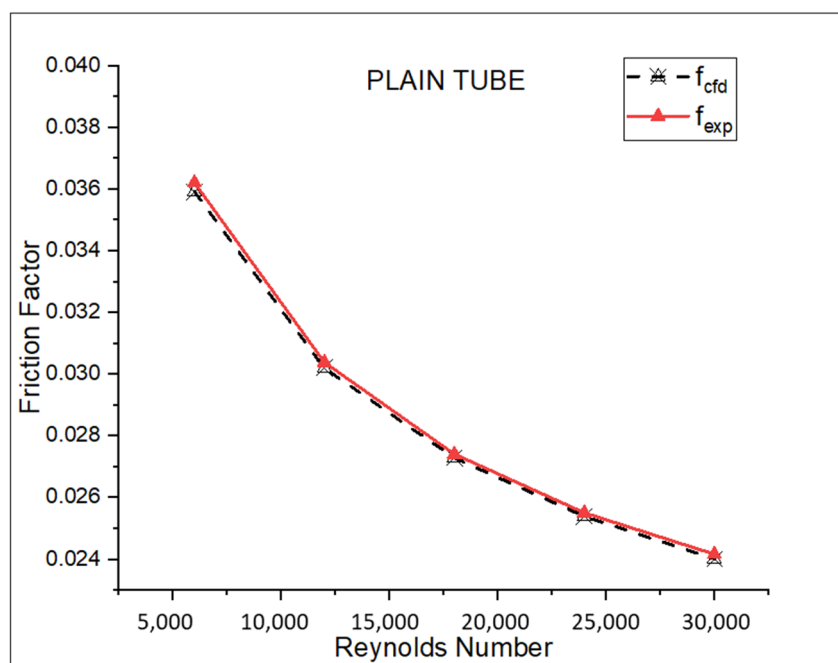


Figure 8. Study of f over Reynolds Number.

The thermal and flow observations were performed for the PWT on different cases as mentioned in Table 6. The case studies are divided based on the three different pitches and para inclinations. Each case is investigated numerically and experimentally for all the flow conditions varying from Reynolds numbers 6000 to 30,000.

Table 6. Experimental/Numerical case studies.

Sl. No.	Designation	Pitch = P	Para-Inclination = PI
1	Plain	—	—
2	Case 1	30 mm = P1	10° PI
3	Case 2	30 mm = P1	15° PI
4	Case 3	30 mm = P1	20° PI
5	Case 4	40 mm = P2	10° PI
6	Case 5	40 mm = P2	15° PI
7	Case 6	40 mm = P2	20° PI
8	Case 7	50 mm = P3	10° PI
9	Case 8	50 mm = P3	15° PI
10	Case 9	50 mm = P3	20° PI

The Nusselt number variation for different cases is shown in Figure 9. The numerical values were seen to be much higher for all the cases for the same condition when compared to the experimental values [41–43]. Each case study was investigated for heat transmission rate in terms of Nusselt number and was compared to the plain tube; the highest Nusselt number was achieved by case studies 2 and 3 with pitch 30 mm and para inclination 15- and 20 degrees. The minimum value of the Nusselt number was observed in case study 7 with a pitch of 50 mm and a para inclination of 10 degrees.

The value of Nu increases with the increase of Re, the turbulators with 15° and 20° inclinations have better augmentation over higher Re because of the development of local turbulence and recirculation to wider openings of inserts. The variation in 10° inclinations has reduced with Re 24,000 to 30,000. The variation of friction factors in different cases is shown in Figure 10. The numerical values were seen to be much higher for all the cases

for the same condition when contrasted with the experimental values [44–46]. Every case study has an appreciation in the friction factor when compared to the plain tube but the highest was achieved by the case study with a pitch of 30 mm and a para inclination of 20 degrees (case 3). The minimum value of the friction factor was experienced by the case studies with a pitch of 50 mm and para inclination of 10 degrees (case 7). The friction factor is higher at low Re and further reduces as the Re increase, the friction factor reduces predominantly from Re 18,000 to 30,000 for a case study with 15° and 20° inclinations, which in turn optimizes Nu.

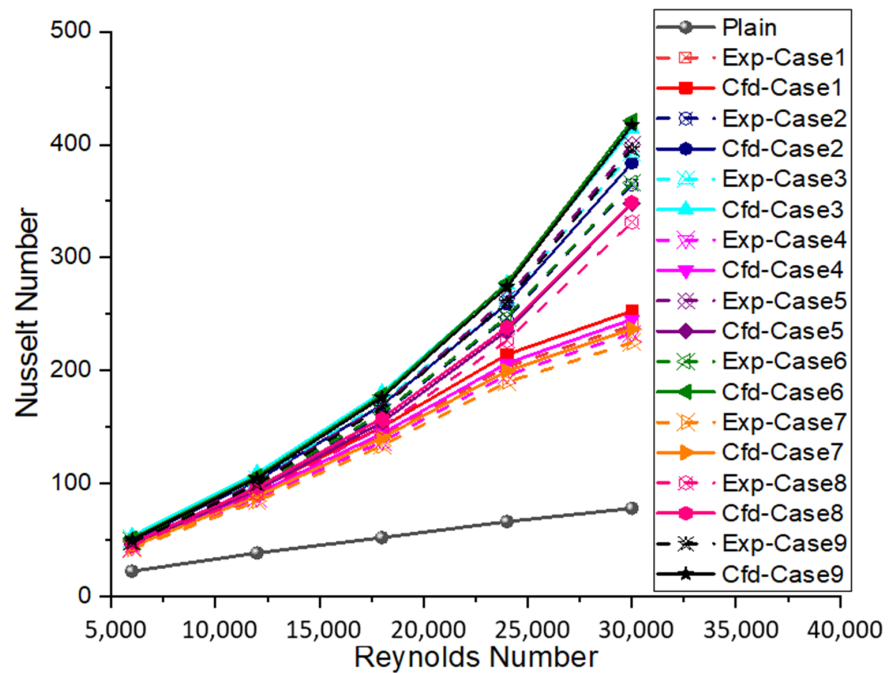


Figure 9. Augmented values of Nusselt Number over Reynolds Number.

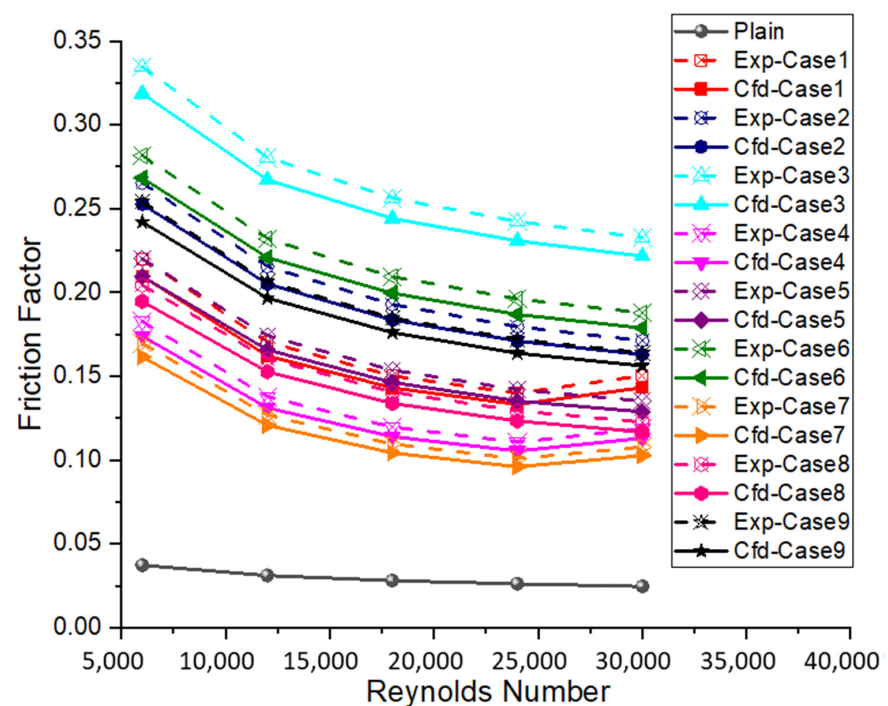


Figure 10. Augmented values of friction factor over Reynolds Number.

Figures 11 and 12 depict the ratio of Nusselt number and Friction factor variations with Reynolds number. Each case study's percentage change in the Nusselt number and friction factor is compared to the plain tube. Reynolds number 30,000 with a para tilt of 20 degrees, the pitch of 40 mm and 50 mm, achieves the maximum Nusselt number ratio (cases 6 and 9). For Reynolds number 30,000, pitch 30 mm and para inclination 20 degrees (case 3), the highest friction factor ratio was achieved. The ratio of Nu increases with the Re, the highest value is attained for pitch 30 mm due to the placement of the maximum number of turbulators within the inner tube, and 20° inclinations due to a wider area of flow restriction which promotes better mixing and recirculation to have better heat transfer. The Nusselt number ratio reduces in those cases with para inclinations of 10° from 18,000 to 30,000 which signifies that, at a greater Reynolds number, para inclinations with 15° with 20° are much better due to local turbulence, and recirculation near the wall boundary.

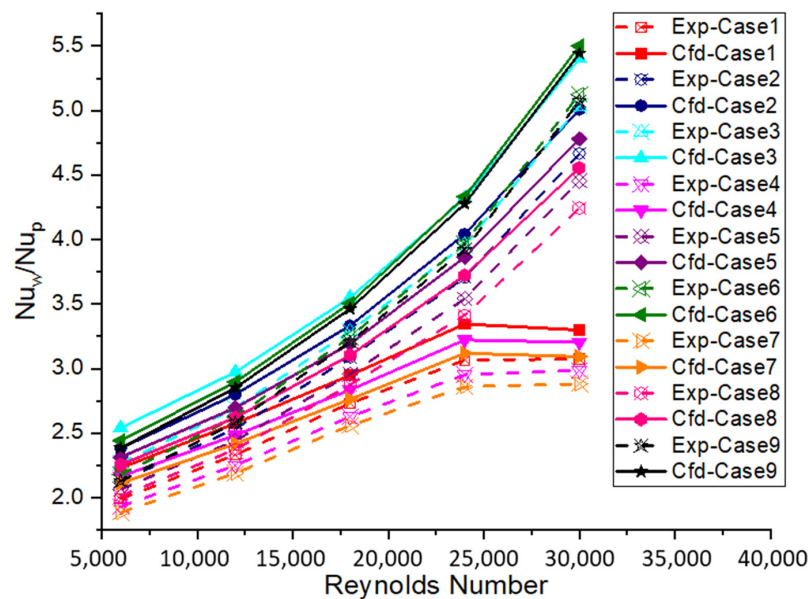


Figure 11. Augmented values of Nusselt Number Ratio over Reynolds Number.

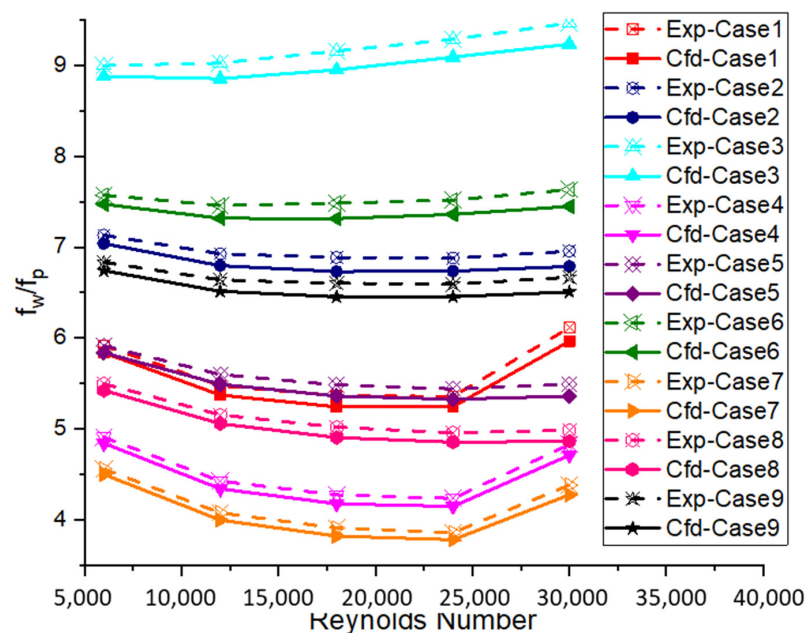


Figure 12. Augmented values of Friction factor Ratio over Reynolds Number.

The lowest value of the Nusselt number ratio is attained for Reynolds number 6000 for pitch 50 mm with para inclination 10 degrees (case 7). The lowest value of friction factor ratio is attained for Reynolds number 24,000 for pitch 50 mm with para inclination 10-degrees (case 7). The ratio of friction factor increases for 20° inclinations irrespective of pitch 30 mm, 40 mm, and 50 mm for Re. The larger pitch and smaller inclination provide the minimum friction factor ratio over Re. The friction factor ratio increases in the cases with para inclinations 10° from 18,000 to 30,000 which signifies that at a greater Reynolds number, para inclinations with 15° with 20° are much better due to better flow distribution over the flow area and streamline flow.

The streamlines of turbulent flow along the PWT for 10°, 15°, and 20° inclinations are shown in Figure 13. The flow lines along PWT inserts represent that the higher the angle of inclination of PWT, the greater the distribution of flow near the wall. The flow at the center follows a zig-zag pattern, near the PWT the flow is distributed, and again at the wall they flow in a straight line.

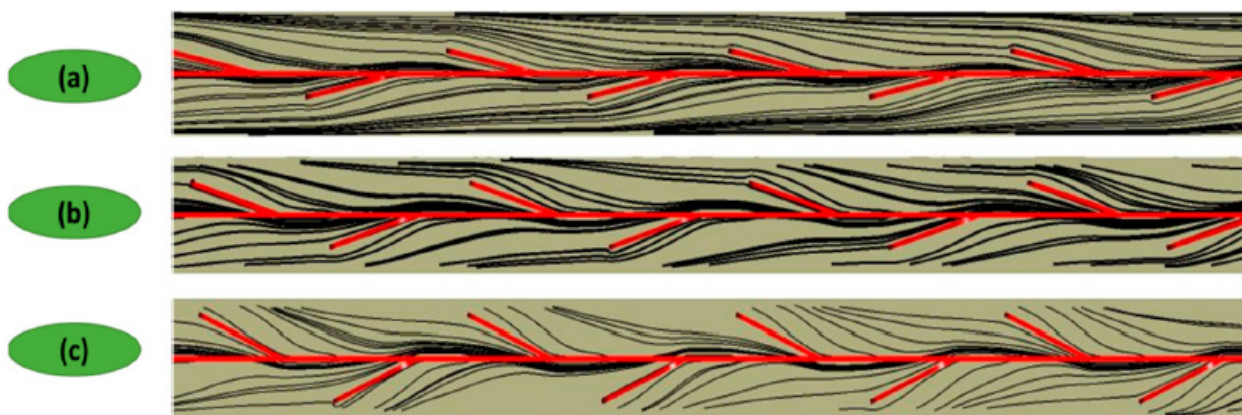


Figure 13. Streamlines along (a) 10°, (b) 15°, and (c) 20° PWT inserts.

The turbulent kinetic energy (TKE) variation in Figure 14 at different inclinations of the PWT shows that due to the application of PWT the TKE intensity near the wall is enhanced and is higher for 20° inclinations. The PWT has created the perfect blend of flow regime with recirculation happening in the form of four quadrants as they pass through the ups and downs of PWT inserts [47–50]. The maximum TKE of 49.61 J/Kg was developed near the edges of the inserts and a minimum of 2.79 was below the insert opening region which creates the recirculation region.

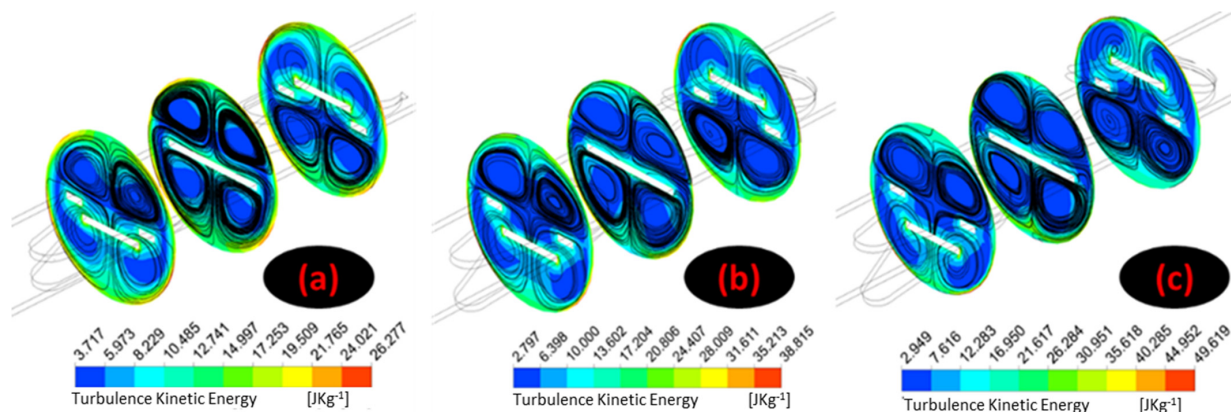


Figure 14. TKE distribution along (a) 10°, (b) 15° and (c) 20° PWT inserts at section x_1 , x_2 and x_3 .

Figure 15 displays the temperature distribution along the plane x_1 , x_2 , and x_3 for various inclinations along 10°, 15°, and 20° for the PWT inserts. The temperature dissemi-

nation along the 20-degree PWT inserts was seen to be much more promising than others. Figure 16 displays the velocity distribution along the x_1 , x_2 , and x_3 planes. For the same Reynolds number, the velocity in the case of 20° inclinations of the PWT inserts is shown to be very high when it comes to other cases [51–53]. The highest velocity is obtained near the corners of the PWT inserts where the recirculation of the flow exits, which is better for mixing and recirculation. From the overall results of Nu, friction factor, TKE, and temperature contours it can be observed that for 20° inclination turbulators, the turbulence regions are widespread due to wider opening area against the flow, for wider openings, the TKE and temperature distribution reached towards the wall boundary layer thereby disturbing and creating better heat transmission along with the heat exchanger.

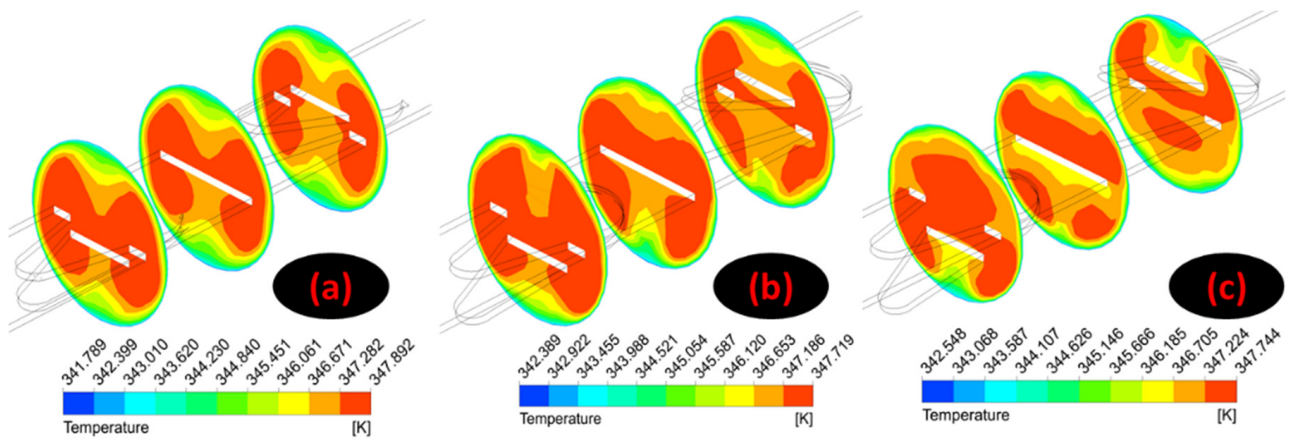


Figure 15. Temperature distribution along (a) 10°, (b) 15° and (c) 20° PWT inserts at section x_1 , x_2 and x_3 .

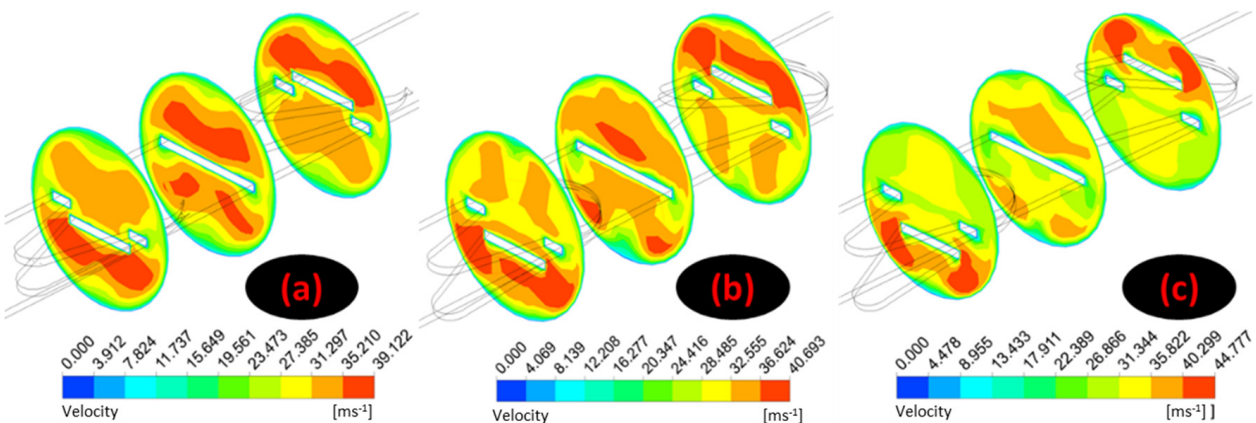


Figure 16. Velocity distribution along (a) 10°, (b) 15° and (c) 20° PWT inserts at section x_1 , x_2 and x_3 .

The performance optimization index (POI) is determined by the ratio of Nusselt number and friction factor. Figure 17a shows the comparison values of POI concerning different case studies of the numerical and experimental studies. The obtained CFD results are within the range of 5% to 8% difference from the experimental values. The maximum POI value of 2.68 to 2.37 was determined experimentally for 20° inclinations from pitch 50 mm to 30 mm. Similarly, 2.91 to 2.57 was determined numerically [53–55]. The minimum POI value of 1.76 to 1.68 was determined experimentally for 10° inclinations from pitch 50 mm to 30 mm. Similarly, 1.9 to 1.81 was determined numerically.

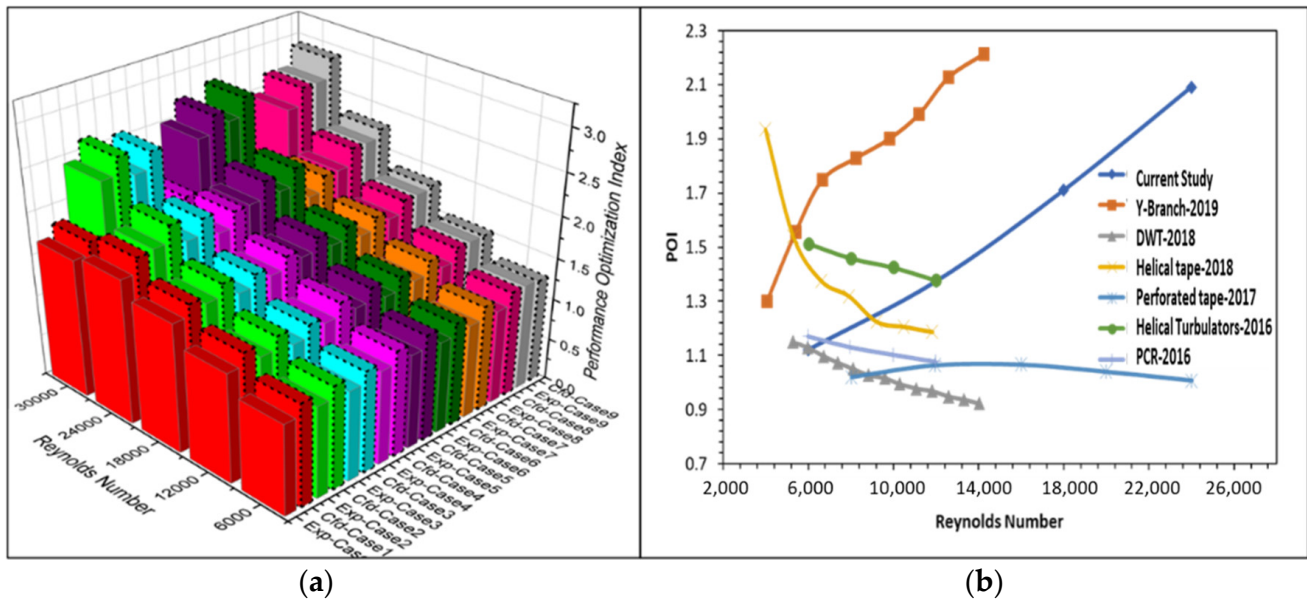


Figure 17. (a) POI of different experimental and computational case studies, and (b) Comparison of POI with present and past investigations.

Finally, the POI shows the overall outcome of the different cases relating to the Reynolds number as displayed in Figure 17a. The comparative study between various other inserts [15–18,20,21] to that of PWT is described in Figure 17b for a better understanding of performance. PWT has good performance at a higher Reynolds number as compared to other inserts except for y-branch inserts.

The model equation for Nusselt number and friction factor are derived from the Reynolds number and the ratio of tube inlet diameter to pitch of the insert (d_i/p) obtained from the test data [29]. Three different d_i/p ratios were examined in this study: 1.62, 2.16, and 2.7. The relation between the observed and projected values of friction factor and Nusselt number is depicted in Figures 18 and 19. The correlation of f and Nu was possible to forecast test values in the range of 6% and 10%, respectively, the constants are also determined and showcased in Equation (3). The performance of the correlations in terms $R^2 =$ coefficient of multiple determination = 0.9944, Standard Error of the Estimate = 5.33, and Proportion of Variance = 99.52%. The constant values of the different case studies of the PWT are presented in Table 7. Uncertainty analyses were carried out in the current investigation to understand the percentage of errors associated with the measuring instruments on various parameters. The analysis follows the procedure described by Kline et al. [39] and Moffat et al. [40]. The error range percentage for data reduction parameters is shown in Table 8. The maximum variation was limited to 5.54% and the minimum was limited to 1.08%.

$$Nu = a(Re)^{(b+1)} \left(\frac{d_i}{p} \right)^c \tag{3}$$

$$f = a(Re)^b \left(\frac{d_i}{p} \right)^c \tag{4}$$

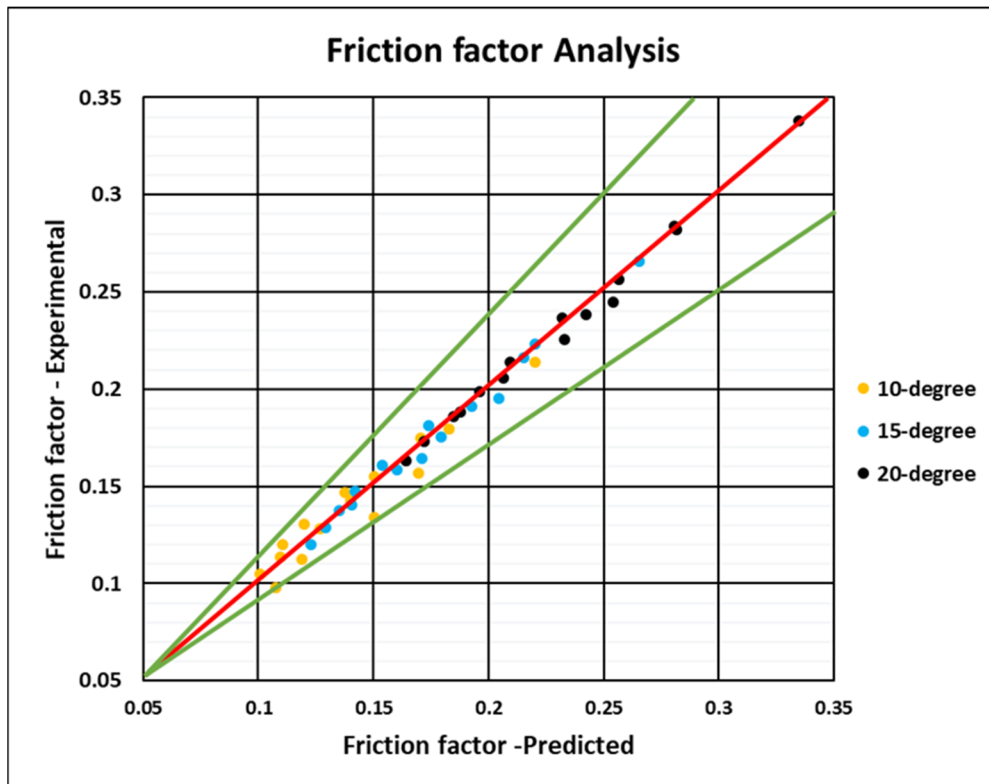


Figure 18. Observed data vs. anticipated data of f .

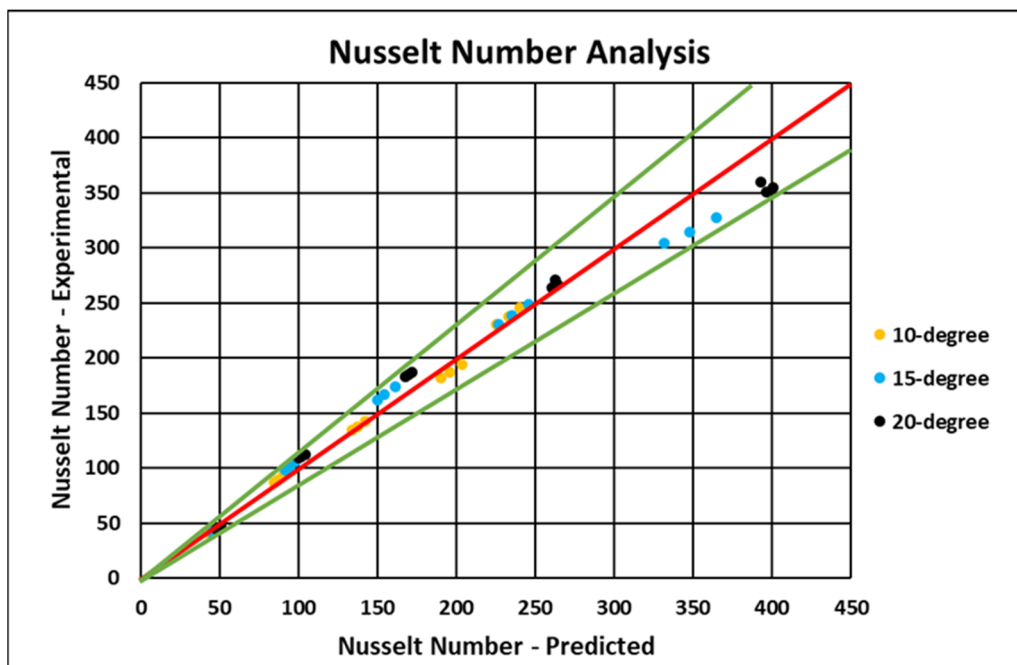


Figure 19. Observed data vs. anticipated data of Nu .

Table 7. Correlation constants of Nu and f .

Case Study	a	b	c
Nu at 10° PI	3.618	−0.2914	−0.6076
Nu at 15° PI	4.866	−0.3004	−0.6076
Nu at 20° PI	4.085	−0.2515	−0.6298
f at 10° PI	4.51×10^{-3}	1.0637	−0.1241
f at 15° PI	1.07×10^{-3}	1.2317	−0.1448
f at 20° PI	7.23×10^{-4}	1.2748	−0.0513

Table 8. Error Range of Experimental parameters.

Sl. No.	Parameters	Error Range (%)
1	Flow rate of hot fluid	1.56–4.89
2	Flow rate of cold fluid	1.52–4.92
3	Reynolds Number	2.04–5.23
4	Pressure drop	1.08–2.03
5	Heat transmission coefficient	1.23–5.15
6	Nusselt Number	1.67–5.42
7	Friction factor	1.89–5.33
8	Temperature	1.04–2.45

6. Conclusions

The performance of PWT as a turbulator to enhance flow and heat transfer was successfully validated with experimental and numerical results of CFD. The variation of Reynolds number, para-inclination and pitch were completely studied on all the flow conditions with the constant temperature at the respective inlet. From the CFD and experimental results it has been seen that the highest value of POI was obtained for case 3, case 6 and case 9, which proves that the higher the para-inclinations, the higher the turbulence kinetic energy, the greater the heat transfer, and the better the POI. The maximum POI value of 2.68 to 2.37 was determined experimentally for 20° inclinations from pitch 50 mm to 30 mm. Similarly, 2.91 to 2.57 were determined numerically. The minimum POI value of 1.76 to 1.68 was determined experimentally for 10° inclinations from pitch 50 mm to 30 mm. Similarly, 1.9 to 1.81 was determined numerically. The empirically obtained Nu and f correlations were built and contrasted with the test data and were found to be within 10% and 6% deviance.

Author Contributions: Conceptualization, T.R., P.R., M.A., S.A.K. and C.A.S.; Data curation, G.K.B.; Investigation, T.R.; Methodology, T.R.; Resources, P.R.; Software, P.R.; Supervision, G.K.B., M.A., S.A.K. and C.A.S.; Validation, G.K.B. and S.A.K.; Writing—original draft, T.R. and G.K.B.; Writing—review & editing, P.R., M.A., S.A.K. and C.A.S. All authors have read and agreed to the published version of the manuscript.

Funding: This research was funded by Universiti Sains Malaysia, Grant No. 1001/PAERO/8014120, and the APC was funded by Universiti Sains Malaysia. King Khalid University, Saudi Arabia.

Institutional Review Board Statement: Not applicable.

Informed Consent Statement: Not applicable.

Data Availability Statement: Not applicable.

Acknowledgments: The authors express their appreciation to The Research Center for Advanced Materials Science (RCAMS) at King Khalid University, Saudi Arabia, for funding this work under the grant number RCAMS/KKU/018-20.

Conflicts of Interest: The authors declare no conflict of interest.

References

1. Shabgard, H.; Allen, M.J.; Sharifi, N.; Benn, S.P.; Faghri, A.; Bergman, T.L. Heat pipe heat exchangers and heat sinks: Opportunities, challenges, applications, analysis, and state of the art. *Int. J. Heat Mass Transf.* **2015**, *89*, 138–158. [[CrossRef](#)]
2. Srimuang, W.; Amatachaya, P. A review of the applications of heat pipe heat exchangers for heat recovery. *Renew. Sustain. Energy Rev.* **2012**, *16*, 4303–4315. [[CrossRef](#)]
3. Huminic, G.; Huminic, A. Hybrid nanofluids for heat transfer applications—A state-of-the-art review. *Int. J. Heat Mass Transf.* **2018**, *125*, 82–103. [[CrossRef](#)]
4. Webb, R. Performance evaluation criteria for use of enhanced heat transfer surfaces in heat exchanger design. *Int. J. Heat Mass Transf.* **1981**, *24*, 715–726. [[CrossRef](#)]
5. Karwa, R.; Sharma, C.; Karwa, N. Performance Evaluation Criterion at Equal Pumping Power for Enhanced Performance Heat Transfer Surfaces. *J. Sol. Energy* **2013**, *2013*, 370823. [[CrossRef](#)]
6. Zimparov, V.D.; Vulchanov, N.L. Performance evaluation criteria for enhanced heat transfer surfaces. *Int. J. Heat Mass Transf.* **1994**, *37*, 1807–1816. [[CrossRef](#)]
7. Liu, S.; Sakr, M. A comprehensive review on passive heat transfer enhancements in pipe exchangers. *Renew. Sustain. Energy Rev.* **2013**, *19*, 64–81. [[CrossRef](#)]
8. Omid, M.; Farhadi, M.; Jafari, M. A comprehensive review on double pipe heat exchangers. *Appl. Therm. Eng.* **2017**, *110*, 1075–1090. [[CrossRef](#)]
9. Alam, T.; Kim, M.-H. A comprehensive review on single phase heat transfer enhancement techniques in heat exchanger applications. *Renew. Sustain. Energy Rev.* **2018**, *81*, 813–839. [[CrossRef](#)]
10. Zheng, N.; Yan, F.; Zhang, K.; Zhou, T.; Sun, Z. A review on single-phase convective heat transfer enhancement based on multi-longitudinal vortices in heat exchanger tubes. *Appl. Therm. Eng.* **2019**, *164*, 114475. [[CrossRef](#)]
11. Mozafarie, S.S.; Javaherdeh, K.; Ghanbari, O. Numerical simulation of nanofluid turbulent flow in a double-pipe heat exchanger equipped with circular fins. *J. Therm. Anal. Calorim.* **2020**, *143*, 4299–4311. [[CrossRef](#)]
12. Liu, P.; Dong, Z.; Lv, J.; Shan, F.; Liu, Z.; Liu, W. Numerical study on thermal-hydraulic performance and exergy analysis of laminar oil flow in a circular tube with fluid exchanger inserts. *Int. J. Therm. Sci.* **2020**, *153*, 106365. [[CrossRef](#)]
13. El Maakoul, A.E.; Laknizi, A.; Saadeddine, S.; Ben Abdellah, A.; Meziane, M.; El Metoui, M. Numerical design and investigation of heat transfer enhancement and performance for an annulus with continuous helical baffles in a double-pipe heat exchanger. *Energy Convers. Manag.* **2017**, *133*, 76–86. [[CrossRef](#)]
14. Kumar, S.; Vasudev Karanth, K.; Murthy, K. Numerical study of heat transfer in a finned double pipe heat exchanger. *World J. Model. Simul.* **2015**, *11*, 43–54.
15. Huang, S.; Zhu, H.; Zheng, Y.; Wan, Z.; Tang, Y. Compound thermal performance of an arc-shaped inner finned tube equipped with Y-branch inserts. *Appl. Therm. Eng.* **2019**, *152*, 475–481. [[CrossRef](#)]
16. Wijayanta, A.T.; Yaningsih, I.; Aziz, M.; Miyazaki, T.; Koyama, S. Double-sided delta-wing tape inserts to enhance convective heat transfer and fluid flow characteristics of a double-pipe heat exchanger. *Appl. Therm. Eng.* **2018**, *145*, 27–37. [[CrossRef](#)]
17. Salem, M.R.; Eltoukhey, M.B.; Ali, R.K.; Elshazly, K.M. Experimental investigation on the hydrothermal performance of a double-pipe heat exchanger using helical tape insert. *Int. J. Therm. Sci.* **2018**, *124*, 496–507. [[CrossRef](#)]
18. Mashoofi, N.; Pourahmad, S.; Pesteei, S. Study the effect of axially perforated twisted tapes on the thermal performance enhancement factor of a double tube heat exchanger. *Case Stud. Therm. Eng.* **2017**, *10*, 161–168. [[CrossRef](#)]
19. Pourahmad, S.; Pesteei, S. Effectiveness-NTU analyses in a double tube heat exchanger equipped with wavy strip considering various angles. *Energy Convers. Manag.* **2016**, *123*, 462–469. [[CrossRef](#)]
20. Sheikholeslami, M.; Gorji-Bandpy, M.; Ganji, D. Effect of discontinuous helical turbulators on heat transfer characteristics of double pipe water to air heat exchanger. *Energy Convers. Manag.* **2016**, *118*, 75–87. [[CrossRef](#)]
21. Sheikholeslami, M.; Gorji-Bandpy, M.; Ganji, D. Experimental study on turbulent flow and heat transfer in an air to water heat exchanger using perforated circular-ring. *Exp. Therm. Fluid Sci.* **2016**, *70*, 185–195. [[CrossRef](#)]
22. Zohir, A.E.; Habib, M.A.; Nemitallah, M. Heat Transfer Characteristics in a Double-Pipe Heat Exchanger Equipped with Coiled Circular Wires. *Exp. Heat Transf.* **2014**, *28*, 531–545. [[CrossRef](#)]
23. Naphon, P.; Suchana, T. Heat transfer enhancement and pressure drop of the horizontal concentric tube with twisted wires brush inserts. *Int. Commun. Heat Mass Transf.* **2011**, *38*, 236–241. [[CrossRef](#)]
24. Zhang, L.; Guo, H.; Wu, J.; Du, W. Compound heat transfer enhancement for shell side of double-pipe heat exchanger by helical fins and vortex generators. *Heat Mass Transf.* **2012**, *48*, 1113–1124. [[CrossRef](#)]
25. Abdelrazek, A.H.; Kazi, S.N.; Alawi, O.A.; Yusoff, N.; Oon, C.S.; Ali, H.M. Heat transfer and pressure drop investigation through pipe with different shapes using different types of nanofluids. *J. Therm. Anal.* **2019**, *139*, 1637–1653. [[CrossRef](#)]
26. Afzal, A.; Islam, T.; Kaladgi, A.R.; Manokar, A.M.; Samuel, O.D.; Mujtaba, M.A.; Soudagar, M.E.M.; Fayaz, H.; Ali, H.M. Experimental investigation on the thermal performance of inserted helical tube three-fluid heat exchanger using graphene/water nanofluid. *J. Therm. Anal. Calorim.* **2021**, *147*, 5087–5100. [[CrossRef](#)]
27. Noorbakhsh, M.; Zaboli, M.; Ajarostaghi, S.S.M. Numerical evaluation of the effect of using twisted tapes as turbulator with various geometries in both sides of a double-pipe heat exchanger. *J. Therm. Anal.* **2019**, *140*, 1341–1353. [[CrossRef](#)]

28. Hosseinejad, R.; Hosseini, M.; Farhadi, M. Turbulent heat transfer in tubular heat exchangers with twisted tape. *J. Therm. Anal.* **2018**, *135*, 1863–1869. [[CrossRef](#)]
29. Thejaraju, R.; Girisha, K.B.; Manjunath, S.; Dayananda, B. Experimental investigation of turbulent flow behavior in an air to air double pipe heat exchanger using novel para winglet tape. *Case Stud. Therm. Eng.* **2020**, *22*, 100791. [[CrossRef](#)]
30. Zolghadri, A.; Maddah, H.; Ahmadi, M.; Sharifpur, M. Predicting Parameters of Heat Transfer in a Shell and Tube Heat Exchanger Using Aluminum Oxide Nanofluid with Artificial Neural Network (ANN) and Self-Organizing Map (SOM). *Sustainability* **2021**, *13*, 8824. [[CrossRef](#)]
31. Menni, Y.; Ameer, H.; Sharifpur, M.; Ahmadi, M.H. Effects of in-line deflectors on the overall performance of a channel heat exchanger. *Eng. Appl. Comput. Fluid Mech.* **2021**, *15*, 512–529. [[CrossRef](#)]
32. Maddah, H.; Ghazvini, M.; Ahmadi, M.H.; Bui, D.T.; Bandarr Filho, E.P. Performance evaluation of a U-shaped heat exchanger containing hybrid Cu/CNTs nanofluids: Experimental data and modeling using regression and artificial neural network. *J. Therm. Anal. Calorim.* **2020**, *143*, 1503–1521. [[CrossRef](#)]
33. Payambarpour, S.A.; Shokouhmand, H.; Ahmadi, M.H.; Assad, M.E.H.; Chen, L. Effect of wetness pattern on the fin-tube heat exchanger performance under partially wet-surface condition. *Therm. Sci. Eng. Prog.* **2020**, *19*, 100619. [[CrossRef](#)]
34. Menni, Y.; Chamkha, A.J.; Ameer, H.; Ahmadi, M.H. Hydrodynamic Behavior in Solar Oil Heat Exchanger Ducts Fitted with Staggered Baffles and Fins. *J. Appl. Comput. Mech.* **2020**, *8*, 774–790. [[CrossRef](#)]
35. Aghayari, R.; Maddah, H.; Pourkiaei, S.M.; Ahmadi, M.H.; Chen, L.; Ghazvini, M. Theoretical and experimental studies of heat transfer in a double-pipe heat exchanger equipped with twisted tape and nanofluid. *Eur. Phys. J. Plus* **2020**, *135*, 1–26. [[CrossRef](#)]
36. Mirzaee, M.; Zare, R.; Sadeghzadeh, M.; Maddah, H.; Ahmadi, M.H.; Acikcalp, E.; Chen, L. Thermodynamic analyses of different scenarios in a CCHP system with micro turbine–Absorption chiller, and heat exchanger. *Energy Convers. Manag.* **2019**, *198*, 111919. [[CrossRef](#)]
37. Chopra, S. Performance study of the electronic and optical parameters of thermally activated delayed fluorescence nanosized emitters (CCX-I and CCX-II) via DFT, SCC-DFTB and B97-3c approaches. *J. Nanostruct. Chem.* **2020**, *10*, 115–124. [[CrossRef](#)]
38. Najafi, F. Thermodynamic studies of carbon nanotube interaction with Gemcitabine anticancer drug: DFT calculations. *J. Nanostruct. Chem.* **2020**, *10*, 227–242. [[CrossRef](#)]
39. Moffat, R.J. Describing the uncertainties in experimental results. *Exp. Therm. Fluid Sci.* **1988**, *1*, 3–17. [[CrossRef](#)]
40. Kline, S.J. The Purposes of Uncertainty Analysis. *J. Fluids Eng.* **1985**, *107*, 153–160. [[CrossRef](#)]
41. Kumar, R.S.V.; Saleh, B.; Sowmya, G.; Afzal, A.; Prasannakumara, B.C.; Gowda, R.J.P. Exploration of transient heat transfer through a moving plate with exponentially temperature-dependent thermal properties. *Waves Random Complex Media* **2022**, 1–19. [[CrossRef](#)]
42. Afzal, A.; Kumar, R.; Jilte, R.; Samee, M.; Shaik, S.; Razak, R.A.; Manokar, A.M.; Saleel, C.A. Numerical analysis and machine learning for battery thermal performance cooled with different fluids. *Int. J. Energy Res.* **2022**, *35*, 1048–1055. [[CrossRef](#)]
43. Murugan, M.; Saravanan, A.; Elumalai, P.; Murali, G.; Dhineshbabu, N.; Kumar, P.; Afzal, A. Thermal management system of lithium-ion battery packs for electric vehicles: An insight based on bibliometric study. *J. Energy Storage* **2022**, *52*, 104723. [[CrossRef](#)]
44. Mujtaba, M.; Cho, H.M.; Masjuki, H.; Kalam, M.; Farooq, M.; Soudagar, M.E.M.; Gul, M.; Ahmed, W.; Afzal, A.; Bashir, S.; et al. Effect of alcoholic and nano-particles additives on tribological properties of diesel–palm–sesame–biodiesel blends. *Energy Rep.* **2020**, *7*, 1162–1171. [[CrossRef](#)]
45. Yaliwal, V.; Banapurmath, N.; Soudagar, M.E.M.; Afzal, A.; Ahmadi, P. Effect of manifold and port injection of hydrogen and exhaust gas recirculation (EGR) in dairy scum biodiesel—Low energy content gas-fueled CI engine operated on dual fuel mode. *Int. J. Hydrog. Energy* **2021**, *47*, 6873–6897. [[CrossRef](#)]
46. Afzal, A.; Khan, S.A.; Saleel, C.A. Role of ultrasonication duration and surfactant on characteristics of ZnO and CuO nanofluids. *Mater. Res. Express* **2019**, *6*, 1150d8. [[CrossRef](#)]
47. Sajadi, A.; Talebi, S. Experimental investigation of heat transfer, pressure drop, and efficiency of TiO₂/Oil nanofluid in alternating flattened tubes. *Energy Equip. Syst.* **2022**, *10*, 123–136.
48. Afzal, A.; Samee, M.; Razak, A. Experimental Investigation of Thermal Performance of Engine Coolant Oil and Water in Helical Coil Heat Exchanger. *J. Eng. Res.* **2019**, *8*, 333–351.
49. Dhairiyasamy, R.; Saleh, B.; Govindasamy, M.; Aly, A.A.; Afzal, A.; Abdelrhman, Y. Effect of particle size on thermophysical and heat transfer properties of Ag nanofluid in a radiator—An experimental investigation. *Inorg. Nano-Metal Chem.* **2021**, 1–15. [[CrossRef](#)]
50. Felemban, B.F.; Essa, F.A.; Afzal, A.; Ahmed, M.H.; Saleh, B.; Panchal, H.; Shanmugan, S.; Elsheikh, A.; Omara, Z.M. Experimental investigation on dish solar distiller with modified absorber and phase change material under various operating conditions. *Environ. Sci. Pollut. Res.* **2022**, 1–12. [[CrossRef](#)]
51. Ziaee, O.; Zolfaghari, N.; Baghani, M.; Baniassadi, M.; Wang, K. A modified cellular automaton model for simulating ion dynamics in a Li-ion battery electrode. *Energy Equip. Syst.* **2022**, *10*, 41–49.
52. Taslimi, M.S.; Dastjerdi, S.M.; Mousavi, S.B.; Ahmadi, P.; Ashjaee, M. Assessment and multi-objective optimization of an off-grid solar based energy system for a Conex. *Energy Equip. Syst.* **2021**, *9*, 127–143. [[CrossRef](#)]
53. Sharifi, M.; Amidpour, M.; Mollaei, S. Investigating carbon emission abatement long-term plan with the aim of energy system modeling; case study of Iran. *Energy Equip. Syst.* **2018**, *6*, 337–349.

-
54. Hajabdollahi, H.; Dehaj, M.S.; Hajabdollahi, H. Investigation of optimization algorithms and their operating parameters in different types of heat exchangers. *Energy Equip. Syst.* **2021**, *9*, 351–370.
 55. Sabzi, S.; Asadi, M.; Moghbelli, H. Review, analysis and simulation of different structures for hybrid electrical energy storages. *Energy Equip. Syst.* **2017**, *5*, 115–129. [[CrossRef](#)]